JTTEE5 17:91–104
DOI: 10.1007/s11666-007-9146-0
1059-9630/$19.00 © ASM International

Mechanical and Thermal Transport Properties of Suspension Thermal-Sprayed Alumina-Zirconia Composite Coatings

Jörg Oberste Berghaus, Jean-Gabriel Legoux, Christian Moreau, Fariba Tarasi, and Tomas Chráska

(Submitted February 27, 2007; in revised form June 29, 2007)

Micro-laminates and nanocomposites of Al_2O_3 and ZrO_2 can potentially exhibit higher hardness and fracture toughness and lower thermal conductivity than alumina or zirconia alone. The potential of these improvements for abrasion protection and thermal barrier coatings is generating considerable interest in developing techniques for producing these functional coatings with optimized microstructures. Al_2O_3-ZrO_2 composite coatings were deposited by suspension thermal spraying (APS and HVOF) of submicron feedstock powders. The liquid carrier employed in this approach allows for controlled injection of much finer particles than in conventional thermal spraying, leading to unique and novel fine-scaled microstructures. The suspensions were injected internally using a Mettech Axial III plasma torch and a Sulzer-Metco DJ-2700 HVOF gun. The different spray processes induced a variety of structures ranging from finely segregated ceramic laminates to highly alloyed amorphous composites. Mechanisms leading to these structures are related to the feedstock size and in-flight particle states upon their impact. Mechanical and thermal transport properties of the coatings were compared. Compositionally segregated crystalline coatings, obtained by plasma spraying, showed the highest hardness of up to 1125 $VHN_{3\ N}$, as well as the highest abrasion wear resistance (following ASTM G65). The HVOF coating exhibited the highest erosion wear resistance (following ASTM G75), which was related to the toughening effect of small dispersed zirconia particles in the alumina-zirconia-alloyed matrix. This microstructure also exhibited the lowest thermal diffusivity, which is explained by the amorphous phase content and limited particle bonding, generating local thermal resistances within the structure.

Keywords abrasive and erosive wear, nanocrystalline composites, solution-precursor TS

1. Introduction

Laminated composites, in which ceramic layers of different compositions and microstructures are combined to obtain properties superior to those of the constituent layer materials, have emerged as an area of extensive research in recent years. Drastic increase in strength and fracture toughness has been achieved in alumina/zirconia laminar composites. The improvements in mechanical behavior are primarily linked to the crack-diverting characteristics of the interlaminate interfaces and the presence of second phases acting as crack arrestors (Ref 1). Other strengthening mechanisms are attributed to the surface residual compressive stresses, which arise from the different thermal expansion coefficients (Ref 2) and elastic moduli of the layers. In alumina/zirconia-layered composites, the strength and toughness have been reported to increase with progressive layer refinement and the introduction of corrugated interfaces (Ref 3, 4). Laminar composites are presently synthesized by different processing routes including tape casting, sequential slip casting, electrophoretic deposition, and colloidal techniques (Ref 5). More recently, physical vapor deposition techniques (PVD) (Ref 6) and thermal spraying have also been used. Thermal spray processing, a technique by which molten ceramic droplet impinge on a substrate and solidify as large disks, i.e., ''splats,'' imparts an inherent lamellar structure, which has been exploited to form alumina-zirconia multilayers (Ref 7) and micro-composites (Ref 8-10). The principal driving force for the development of thermal-sprayed Al_2O_3/ZrO_2 composites is to enhance the resistance against abrasion, wear, and oxygen diffusion, as well as the thermal resistance of thermal barrier coatings (TBCs) over conventional stabilized zirconia in the high-temperature environment of turbine engines. The combination of high hardness of alumina with the low thermal conductivity of zirconia may lead to next generation TBCs with improved properties and service life. Besides creating thin alternating layers, the rapid solidification of the molten ceramics in the thermal spray process can, in some cases, extend the solid solution of zirconia in alumina to form metastable amorphous phases. This is most easily accomplished at a composition of 57% Al_2O_3-43% ZrO_2,

Jörg Oberste Berghaus, Jean-Gabriel Legoux, and **Christian Moreau**, Industrial Materials Institute, NRC, Boucherville, QC, Canada; **Fariba Tarasi**, Concordia University, Montreal, QC, Canada; and **Tomas Chráska**, Institute of Plasma Physics, ASCR, Praque, Czech Republic. Contact e-mail: jorg.oberste-berghaus@cnrc-nrc.gc.ca.

since the binary phase diagram features a eutectic point with lowering of the liquid curve to 1900 °C (Ref 11, 12). A nanocomposite structure can arise from this metastable amorphous phase by the nucleation of ZrO_2 crystals in the Al_2O_3 matrix during postannealing (Ref 13-15). Similar to the laminates, the nanocomposites can show improvements in thermal resistance and mechanical properties compared to both alumina and zirconia, i.e., higher fracture toughness (Ref 13, 16). In fact, the ZrO_2/Al_2O_3 bulk composite is a classical model of a transformation-toughening ceramic system (Ref 6). The toughening effect is most often explained in terms of an alumina matrix, which exerts local compressive stresses around small zirconia crystals, hindering the martensitic phase transformation from tetragonal to monoclinic ZrO_2 (Ref 16).

Thermal spraying of liquid feedstock, using either precursor salts in solution (Ref 17-19) or particle suspensions (Ref 20-22), are emerging technologies for the production of finely structured functional layers and can yield unique microstructures (Ref 23, 24) and phase compositions (Ref 25) in Al_2O_3-ZrO_2 composites.

In this work, microlaminate composites of alumina/zirconia are produced by suspension thermal spraying of submicron feedstock powders. The liquid carrier employed in this approach allows for controlled injection of much finer particles than in conventional thermal spraying, leading to a high degree of structural refinement in the coatings. The effects of spray conditions and feedstock nature are explored to either foster a structure of finely alternating ceramic layers or the creation of amorphous/nanostructured constituents. Two different thermal spray systems were employed, an axial injection plasma torch and a high-velocity oxyfuel (HVOF) gun. A wide diversity in coating microstructure is expected from the two very different spray systems. Mechanical properties and thermal conductivities of the coatings are evaluated. The ultimate goal is to delineate how to tailor the unique microstructures obtained by suspension thermal spraying for meeting desired mechanical and thermal transport property requirements.

2. Experimental Procedure

2.1 Suspension Spray Equipment and Operation

Suspension spraying was implemented for an axial injection plasma torch Mettech Axial III (Northwest Mettech Corp., North-Vancouver, BC, Canada) and a HVOF DJ-2700 Hybrid gun (Sulzer-Metco, Westbury, NY, USA). The systems were equipped with internal injection and twin-fluid atomization modules. The co-axially fed suspension droplets are fully entrained by encircling three plasma streams, as in the case of the Mettech Axial III torch, or are intimately contacted with the fuel inside the HVOF combustion chamber, as in the case of the DJ-2700 gun. Such arrangements can reduce the process sensitivity to the injection conditions and are expected to yield a high degree of heat and momentum transfer from the jets. The suspensions were delivered by a specialized feeding system, using a positive-displacement dosing pump and precision flow meters. Start-up, shutdown, and rinsing sequences were fully automated and PC controlled. The plasma torch was operated at three selected conditions of gas flow rate, gas composition, and exit nozzle sizes, which were previously used to produce continuous, dense, and well-adhering coatings and which are summarized in Table 1. Nitrogen at a flow rate of 10 slpm was employed as the atomizing gas. A spray distance of 51 mm between the torch exit nozzle and the substrate was maintained throughout during coating fabrication.

Table 1 Plasma operating conditions

Spray condition	Exit nozzle, mm	Torch current, ×3	Gas flow, slpm	Power, kW	Ar, %	N_2, %	H_2, %
1	11 (7/16 in.)	180 A	180	84	45	45	10
2	9.5 (3/8 in.)	180 A	180	86	45	45	10
3	9.5 (3/8 in.)	200 A	245	82	75	10	15

Torch traverse speed: 600 mm/s (24 in./s); Atomizing gas N_2 at 10 slpm

Table 2 HVOF spray parameters for ceramic A40Z feedstock suspension, DJ 2700

Parameter	Value
Propylene flow	85 slpm
Oxygen flow	279 slpm
Air flow	202 slpm
Carrier gas (N_2) flow	17 slpm
Suspension feed rate	55 mL/min (3.1 kg/h)
Spray distance	12.7-15.2 cm
Gun traverse speed	30 in/s

The spray parameters for the DJ 2700 HVOF gun are listed in Table 2. These conditions, with over stoichiometric oxygen flow, were selected to yield a high flame temperature and heat output of this equipment, while limiting the backpressure in the combustion chamber during spraying to approximately 620 kPa (90 psi).

In-flight particle states were measured with a commercial diagnostic system (AccuraSpray® G2 and G3, Tecnar Automation, St-Bruno, PQ, Canada). Since the small size of the particles prevents individual in-flight particle detection, an ensemble particle diagnostic system, which senses the fluctuations of the total emitted radiation in the field of view, is deemed necessary (Ref 26). The temperature measurement is based on two-color pyrometry, and the velocity is determined by a time-of-flight technique. The measurement volume was centered in the spray plume at the location of the substrate during deposition.

2.2 Coating Characterization

Microstructures of the coatings were observed by SEM (JEOL JSM-610) and FE-SEM (Hitachi S4700). The samples were sectioned using a precision saw, mounted under vacuum in epoxy resin, and prepared by standard

metallographic methods to produce a polished cross section. Porosity was assessed on the cross section by SEM (500 and 5000 magnification) using image analysis. The intensity range and thresholds were standardized on reference materials, and 10 measurements were averaged per sample. This method at 500 times magnification is well suited to rank porosities of conventional thermal spray coatings and well describes the occurrence of large defects in the present coatings. Evaluation at 5000 magnification was attempted to capture some of the finer porosity and nanopores encountered in this study.

Vickers microhardness measurements were performed under a 3 N load for 20 s on the polished cross section of the coatings. A total of 10 measurements were taken per sample. The relative toughness of the material was estimated from the crack propagation resistance, as determined from the average crack length ($2c$) originating from the corners of the Vickers indentation impression at a load (P) of 3 N. The relationship $P/c^{3/2}$, where P is in Newtons and c in meters, was employed in this comparison (Ref 27). An average of 10 indents were used per sample.

Abrasion resistance of the coatings under dry conditions was tested based on the ASTM standard method G65-00 (procedure D-modified), also known as the dry sand/rubber wheel test (Ref 28). A coated sample is pressed against a rotating rubber wheel (200 rpm) with a force of 45 N. Silica sand (212-300 μm) is fed between the coating and the wheel, until the wheel has traveled an equivalent linear distance of 1436 m (2000 rev.). The lighter load variation of the standard procedure allowed ranking of the relatively thin coating material. Prior to the test, the coatings were faced to a level surface. The volume loss was measured by optical profilometry.

Erosion resistance by solid particle impingement was evaluated based on the ASTM standard method G76-83, exposing a coated sample to 100 grit alumina particles (standard 122 μm average and 203 μm maximum), which impact with a speed of 64 m/s at an angle of 30° (Ref 29). The test duration was 30 s with a particle feed rate of 3.86 g/min. The volume loss at the erosion scar was measured by optical profilometry.

Thermal diffusivity α was evaluated for selected samples using a laser flash method (Ref 30). For each spray condition, three replicate samples were analyzed with at least five heating cycles. To ensure absorption of the laser radiation at the coating surface, the samples were coated with palladium. The thermal conductivity k of these coatings was determined using the relationship $k = \alpha C_p \rho$. Specific-heat (C_p) measurements for Al_2O_3-ZrO_2 coatings are made using a standard differential scanning calorimeter (DSC-2, Perkin-Elmer, Fremont, CA, USA), with sapphire as a reference material. Material density was approximated by a linear law of mixing, neglecting porosity.

Phase analysis was carried out by XRD using a Brucker D8-Discovery diffractometer (Brucker AXS Inc., Madison, WI, USA) with Cu-K_α radiation at an acquisition of 0.01°/s. The crystallite size was approximated from the Sherrer equation at the principal diffraction lines (Ref 31). An attempt was made to quantify the degree of crystallinity by measuring the area of crystalline peaks between 25° and 40° vs. the total integrated area in this region, including the diffuse amorphous hump. This index reflects the alloying of the ceramic constituents into an amorphous phase due to rapid solidification and allows here a qualitative comparison between the coatings obtained at different spray conditions.

Particle sizes and distribution were measured with a Coulter LS Laser Particle size analyzer (Beckman-Coulter, Mississauga, ON, Canada) using the Universal Liquid Module, characterizing the powders and powder agglomerates as they are present in the suspension.

2.3 Materials and Suspensions

Two different feedstock particle sizes were used in this study, namely nanosized (<80 nm), NA, and slightly larger superfine powders (SF). NA denotes feedstocks of nanosized alumina mixed with nanosized zirconia. SF denotes mixtures of the larger superfine alumina and zirconia powders. The distinction between nanosized and superfine particles is somewhat arbitrary, but allows here to differentiate between the powders. The constituents Al_2O_3-ZrO_2-Y_2O_3 were mixed with weight ratios of 57-42-1 (NA), 60-40-0 (NA-HVOF), and 60-40-0 (SF), which are close to the eutectic composition. YSZ powder (3 mole% yttria-doped ZrO_2) without the addition of alumina was also used for reference purposes. The four different powder mixtures and the corresponding constituents are summarized in Table 3. The morphologies and phase

Table 3 Summary of feedstock powders

Feedstocks	Wt.%	Powders	Nominal particle size, nm	Specific surface area, m^2/g
NA	57 (60)	α-Al_2O_3	27-43	35 (a)
	21.5 (40)	*m*-ZrO_2	29-68	35 (a)
	21.5 (0)	3 mol% YSZ	58-76	17.5 (a)
NA-HVOF	60	α-Al_2O_3	27-43	35 (a)
	40	*m*-ZrO_2	29-68	35 (a)
YSZ	100	3 mol% YSZ	58-76	17.5 (a)
SF	60	α-Al_2O_3	390	8.0 (b)
	40	*m*-ZrO_2	300-700	15 (c)

(a) Nanostructured & Amorphous Materials, Houston TX, USA
(b) Malakoff Industries, Malakoff TX, USA
(c) Inframat Advanced Materials, Farmington CT, USA

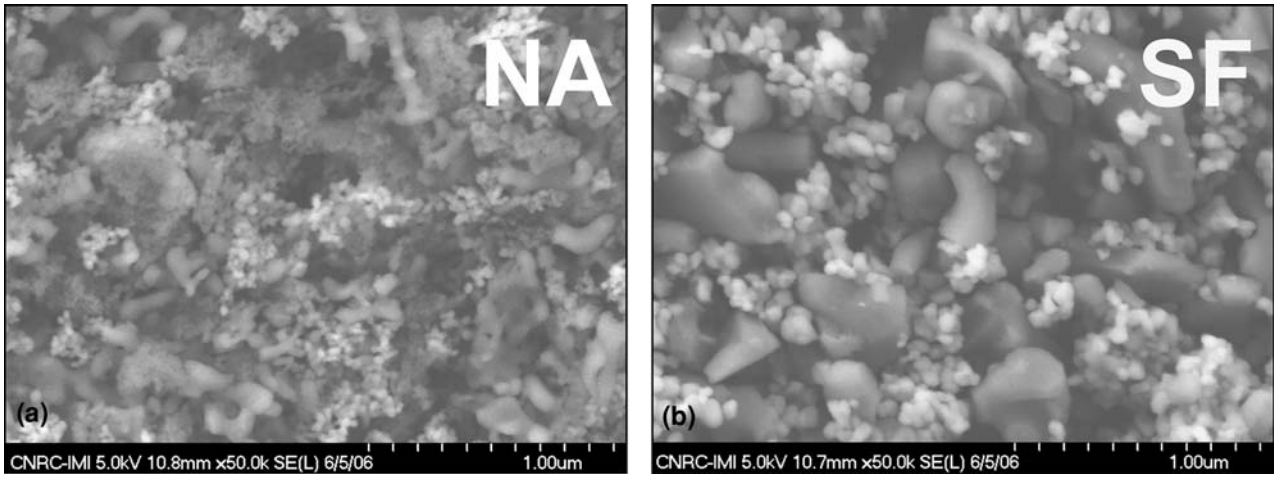

Fig. 1 Micrographs of the ball-milled Al_2O_3-ZrO_2 feedstock showing mixing of (a) nanosized particles of Al_2O_3 (*dark*) and ZrO_2 (*light*) and (b) superfine particles of Al_2O_3 and ZrO_2

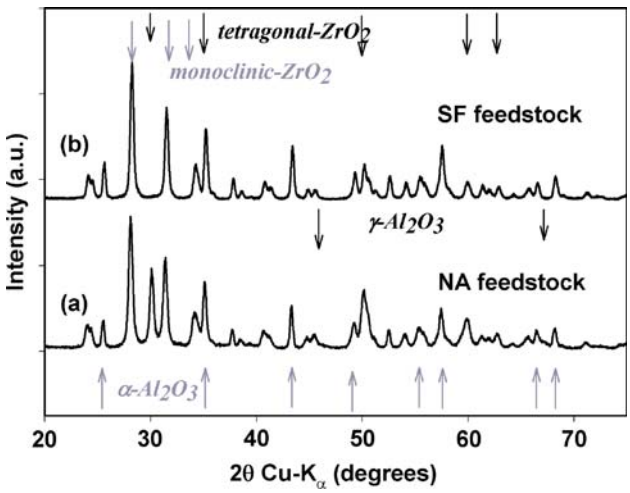

Fig. 2 XRD spectra of feedstock powders

composition of the feedstock were verified by high-resolution FE-SEM and XRD, shown in the micrographs in Fig. 1 and the spectra in Fig. 2.

Suspensions were prepared with 5 wt.% solids in ethanol for HVOF and 10 wt.% solids for plasma spraying. Polyethylenimie (PEI) (0.6 wt.% per solids) (MWT 25,000, Alfa Aesar, Ward Hill, MA, USA) was used as a dispersing agent. This cationic polyelectroyte adsorbs on the ceramic surfaces and can be charged positively by protonation of the amine groups, i.e., by adjusting the pH to less basic conditions. Low-energy ball milling was needed to break up the initial particle agglomerates and to ensure mixing of the constituents. The suspensions were subjected to milling at 140 rpm for 24 h using zirconia media in polyethylene jar mills. After milling, the suspensions were diluted to the desired solid content and further dispersed in an ultrasonic bath. The procedure outlined above stabilized the dispersion sufficiently to be compatible with the spray process. It should be pointed out that this procedure is insufficient to maintain monodispersed suspensions. The size distributions of the particles in suspension are shown in Fig. 3. The finer NA powder shows large agglomerates with a median size of 6 μm and no individual submicron particles, while the SF feed shows smaller aggregates (median 2 μm) and a high portion of submicron particles.

2.4 Substrate Considerations

Coatings were produced on mild steel substrates with dimension of 25 mm × 75 mm × 12.5 mm. To increase coating adhesion, the substrate surface was grit blasted with 60 grit (standard 254 μm average and 406 μm maximum) Al_2O_3 particles prior to deposition, yield a surface roughness of approximately 4.5 μm R_a. In order to maintain a substrate temperature below 450 °C during deposition, backside cooling using both compressed air and water was implemented. An attempt was made to reduce air front cooling, whereby high-velocity air jets are directed toward the front of the substrate surface, which was observed to deflect the particle jet and poses the risk of adversely affecting the resulting coating.

3. Results and Discussion

3.1 Processing Conditions and Particle States

Measured particle states for selected feedstocks and operating conditions are summarized in Table 4. For the suspension plasma spraying using the nanosized feedstock, the effect of processing conditions is illustrated in samples NA-1 through NA-3. With smaller nozzle size and increase in gas flow rate (NA 1 to NA 3) particle velocities close to 700 m/s could be generated. In the case of sample SF-3, nearly 800 m/s have been reached. These high particle velocities are somewhat unusual for plasma spraying, but can be rationalized in terms of a low inertia of the small particles. The smaller the particles, the more

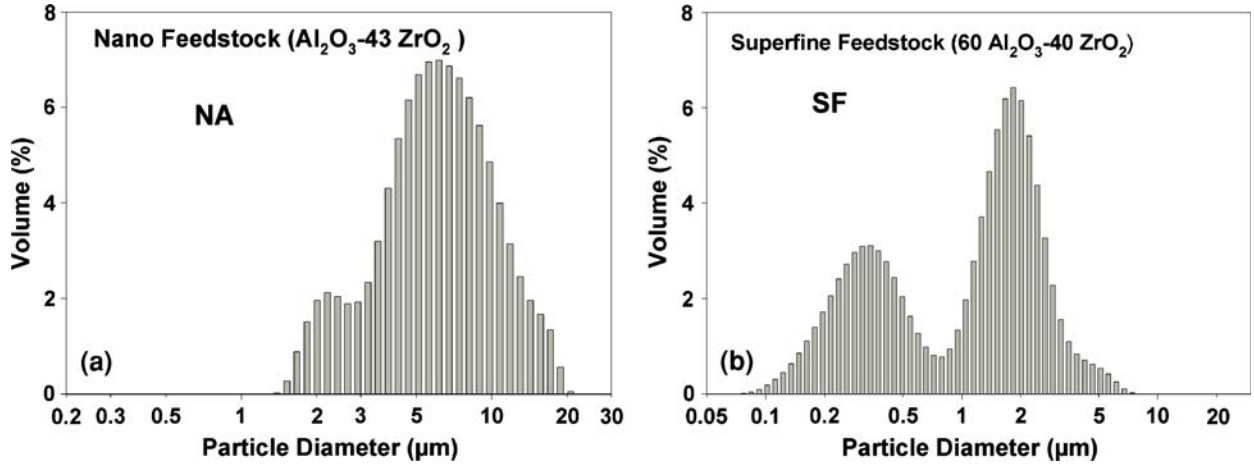

Fig. 3 Aggregate size distribution in feed suspensions as measured with a Coulter LS Particle size analyzer for (a) nanosized powder mixture NA and (b) superfine powder mixture SF

Table 4 Operating conditions and particle states

Sample	Plasma/HVOF condition	Feed rate, kg/h	SD, mm	V_{part}, m/s	T_{part}, °C
NA-1	1	1.8	50	500	2860
NA-2	2	1.4	50	620	2937
NA-3	3	1.1	50	690	2750
SF- 3	3	1.1	50	774	2760
NA-HVOF	HVOF	3.1	127	740	2814
YSZ	2	1.4	50	640	2980

intimately they follow the gas flow velocity as they are entrained in the plasma stream (Ref 26). Previous work has, however, shown that these high velocities do not necessarily translate into high impact velocities on the substrate (Ref 26). The same low inertia, readily accelerating the particles in the jet, slows the particles in the stagnation point above the substrate. For the same particle size, however, faster free stream conditions lead to higher impact velocities.

It was also generally observed that the high velocities come at the expense of a reduced particle temperature, possibly due to a shorter residence time of the particles in the heating plasma jet. The suspension feed rate, affecting the thermal load on the plasma, was reduced in those cases to maintain the particle temperatures above the melting point of the refractory ceramic, i.e., at least above 2700 °C for zirconia (see Table 4).

The high particle temperatures measured for the HVOF system, i.e., above the melting point of zirconia, are somewhat surprising, considering the much lower flame temperatures, as compared to plasma. The larger surface area and the smaller thermal mass of the submicron particles may lead to improved heat absorption and facilitate heating and melting. The long residence time of the particles in the flame may also play a role. It should be mentioned that only the particle surface temperature is captured by the optical diagnostics, while the particle cores may actually be colder.

3.2 Coating Structure and Phase Composition

Typical microstructures of the coatings are shown in Fig. 4, 5, and 6. Depending on the operating conditions and feeding rates, deposition rates varied from 3 to 5 μm/pass. Coatings up to 600 μm in thickness were produced. Table 5 shows porosities of approximately 2% as evaluated from image analysis at a magnification of 500. The bulk regions of the coatings are significantly denser with porosities below 1%, as evaluated at a magnification of 5000. However, for some conditions the coatings feature large cone-shaped defects delimited by porous regions, which grow as the films gain thickness. The cones terminate as surface bumps. These defects may arise by virtue of the low inertia of the small particles and were also observed by other authors for small particles plasma-sprayed alumina coatings (Ref 32). The root cause for these structures may lie in the turning trajectory of some small particles, which carry little momentum to properly impact and spread on the substrate. Earlier work has shown that these particles, contained within the particle jet, intimately follow the radially deflecting gas flow in the stagnation point above the substrate (Ref 26). Instead of impacting with a high normal velocity, those particles travel laterally along the substrate surface and possibly attach on asperities comprised in the surface roughness, creating a region of porosity and build-up. The growing cones then further shadow the underlying pores from the normal impacting particles (Ref 33). On the other hand, high particle velocities can decrease the portion of deflecting particles to smaller sizes and lower numbers. During the course of the experiments, many other process parameters were observed to promote these structures. Some of these are: a high surface roughness leading to early defect formation by providing asperities for particle attachment; a large substrate size and a diverting plasma jet, exposing the coating to the periphery of the particle jet, which preferentially contains the smallest particles, to name a few. An attempt has been made here to minimize the extent of these defects for each feedstock and process,

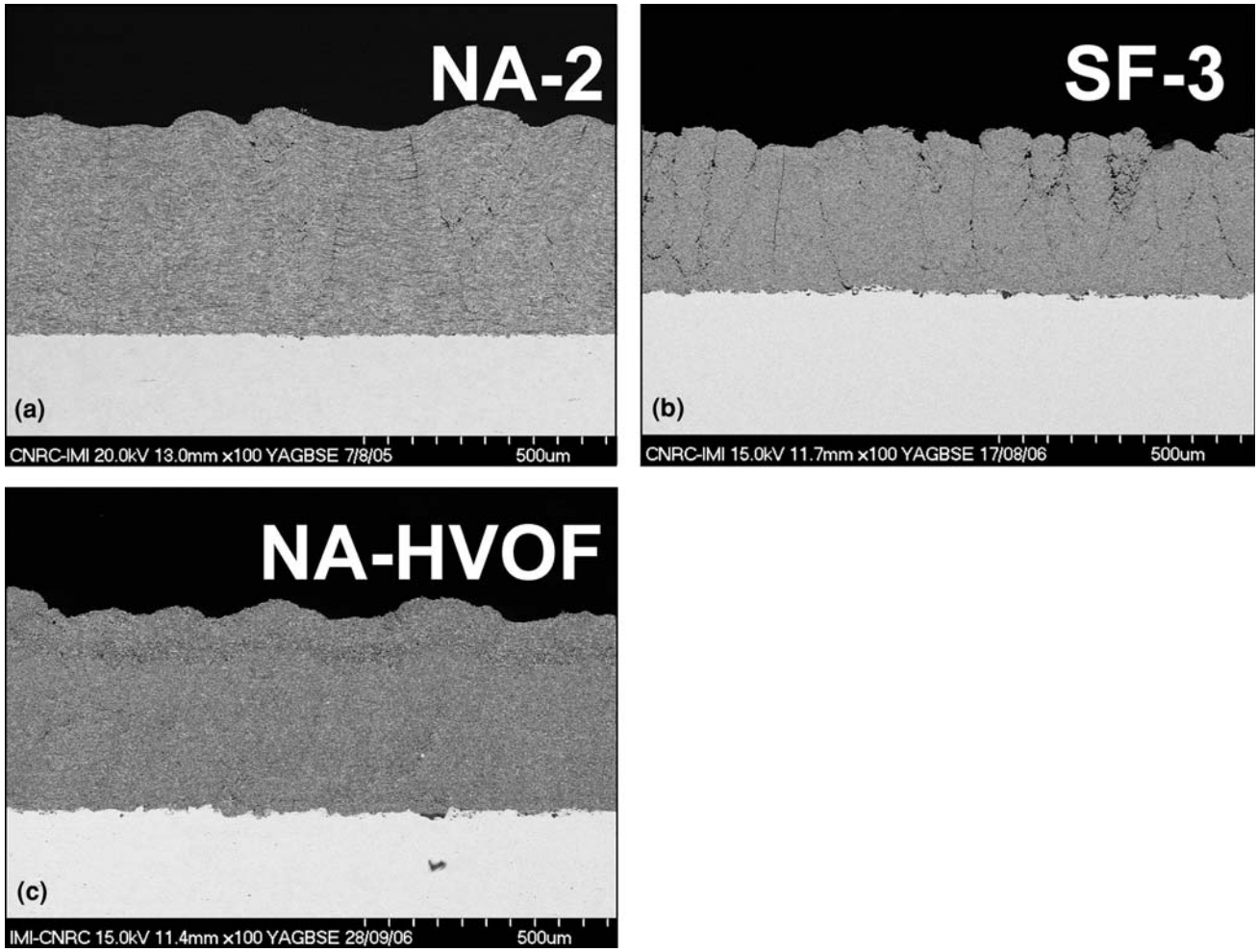

Fig. 4 Cross section micrograph of coating (a) plasma-sprayed coating from nanosized feedstock NA-2, (b) plasma-sprayed coating using superfine feedstock SF-3, and (c) HVOF-sprayed coating using nanosized feedstock NA-HVOF, all showing a dense structure with cone-shaped regions of porosity and cracks

and to compare only optimized coatings of porosities around or below 2%.

XRD spectra of the selected coatings are shown in Fig. 7. Phase composition and grain sizes are summarized in Table 5. The plasma-sprayed coatings from the nanosized feedstock (NA-1 to NA-3) feature a high degree of crystallinity dominated by the metastable t'-ZrO_2 and γ-Al_2O_3 phases. The grain sizes in these phases are approximately 20-30 nm. The small volume of the liquid ceramic droplets likely restricts the grain growth during the rapid solidification, which leads to nanostructured coatings and retention of the metastable phases (Ref 24).

The micrographs of the NA coatings in Fig. 5(a) and 6 show a fine lamellar structure of alternating alumina and zirconia layers. A small amount of intimate mixing of the components can be identified in the gray halo regions in the vicinity of the zirconia splats, which may indicate the presence of some amorphous phase. This phase remains, however, undetectable within the resolution of the XRD spectra. A possible mechanism, leading to this phase segregation will be suggested later. The microstructures of the NA coatings are all very similar. However, at higher particle velocity (NA-1 to NA-3), more of the smallest particles are incorporated into the coating, leading to a refinement in the layer structure, as can be seen by comparing Fig. 6(a), 5(a), and 6(b). The high velocity and lower particle temperature in NA-3 may also foster the deposition of small in-flight solidified particles, leading to some retention of the α-Al_2O_3 phase (Table 5).

Contrary, the coatings from the submicron feedstock (SF-3) are dominated by gray lamellar of intermediate contrast, i.e., alloyed Al_2O_3-ZrO_2 composite. Indeed, an amorphous phase content of 55% was estimated by XRD, see Table 5. In spite of the lack of yttria for chemical stabilization, only the metastable tetragonal phase can be identified. Furthermore, the t'-ZrO_2 grain size of 14 nm is considerably lower than in the NA coatings. This may suggest the formation of a nanocomposite whereby the t'-ZrO_2 crystallites are stabilized by the constraining Al_2O_3 matrix, as explained earlier.

The microstructure of the HVOF coating is most complex and shows Al_2O_3 and Al_2O_3-ZrO_2-alloyed

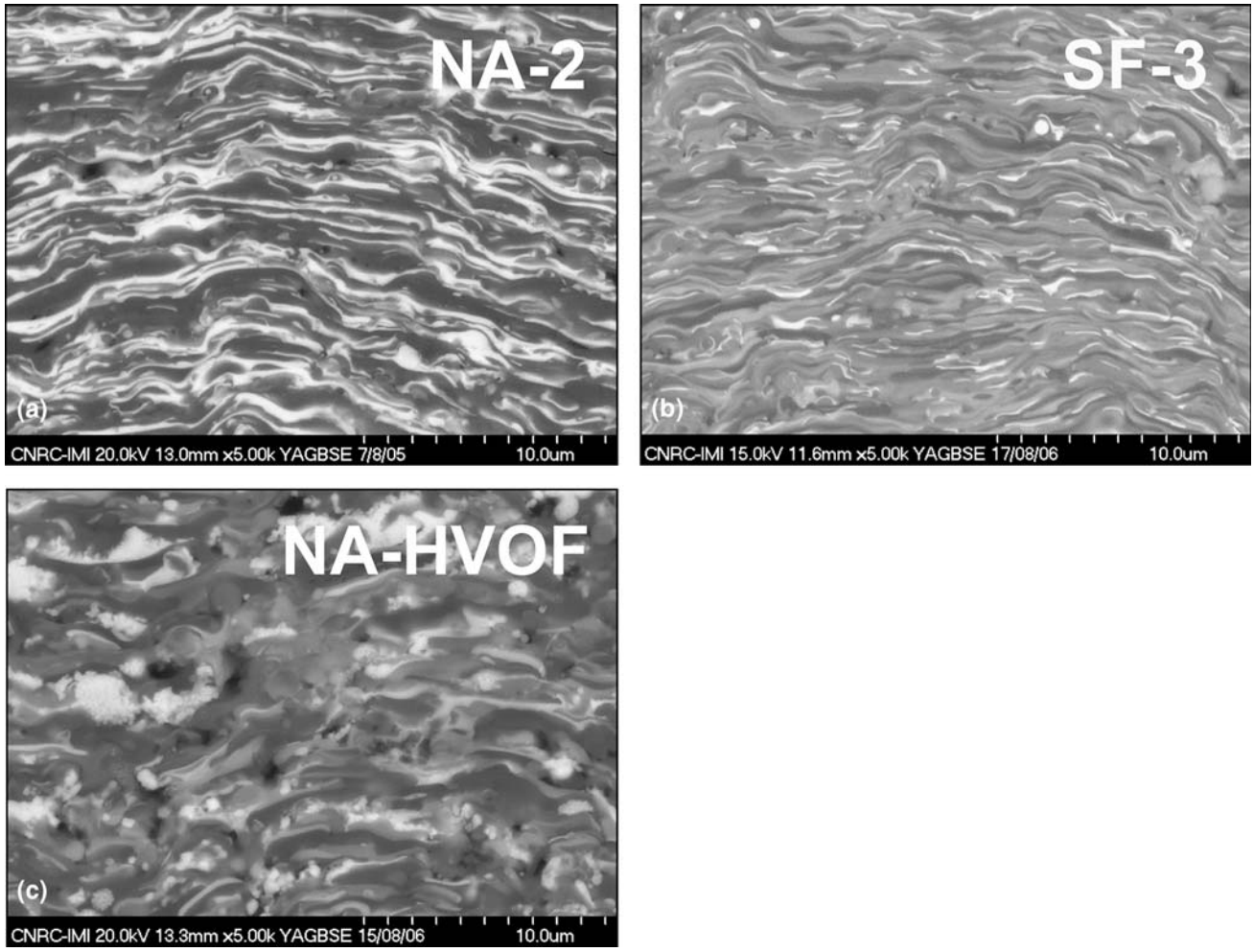

Fig. 5 Cross section micrograph of (a) plasma-sprayed coating from nanometric feedstock NA-2, showing distinct lamellar structure (b) plasma-sprayed coating using superfine feedstock SF-3, showing amorphous Al_2O_3-ZrO_2 pseudo-alloyed lamellar structure, and (c) HVOF-sprayed coating using nanometric feedstock NA-HVOF, showing a complex lamellar structure containing amorphous Al_2O_3-ZrO_2 pseudo-alloyed and embedded unmelted clusters of submicron zirconia particles

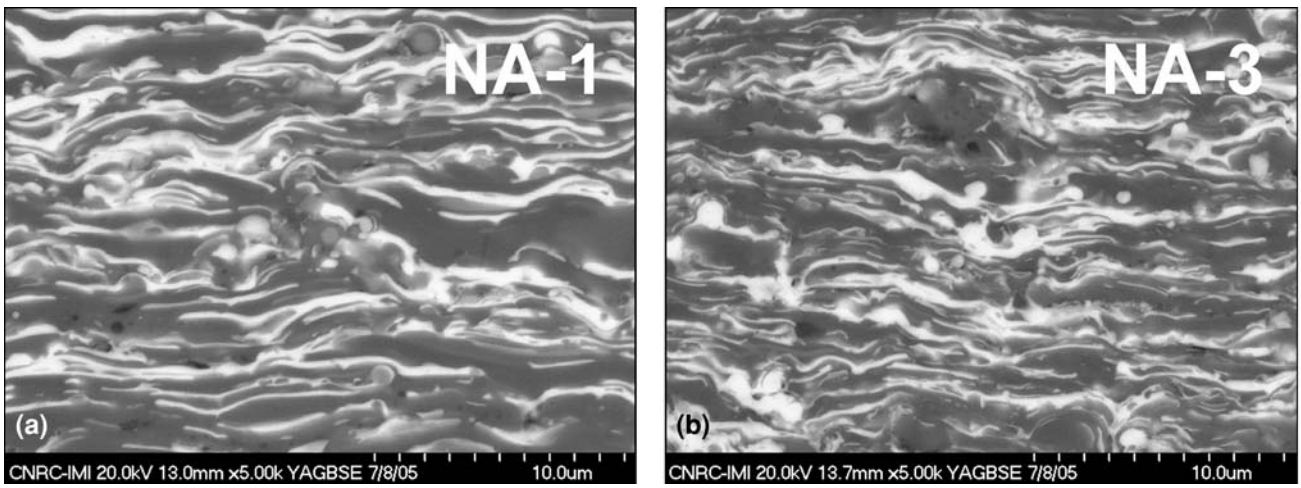

Fig. 6 Microstructures of (a) NA-1 and (b) NA-3, showing distinct compositional layers of Al_2O_3 (*dark*) and ZrO_2 (*light*), and increasing layer refinement with particle velocity

Table 5 Summary of porosities and XRD phase analysis

Condition	Porosity, %		Phase content, %		Grain sizes, nm				Amorphous phase, %
	500×	5000×	m-ZrO_2 $\left(\frac{m}{m+t}\right)$	α-Al_2O_3 $\left(\frac{\alpha}{\alpha+\gamma}\right)$	m-ZrO_2	t'-ZrO_2	α-Al_2O_3	γ-Al_2O_3	
NA-feed			63	100	25	28	61	···	···
SF-feed			100	69	38	···	66	84	···
NA-1	1.9 ± 1.0	1.07	20	0	22	25	···	26	···
NA-2	1.5 ± 1.1	0.46	14	0	23	23	···	26	···
NA-3	1.3 ± 0.6	0.92	12	20	28	24	85	25	···
SF-3	1.7 ± 0.8	0.13	0	31	···	14	34	24	55
NA-HVOF	0.9 ± 0.6	0.17	12	43	30	31	72	32	48
YSZ	2.3 ± 0.9	0.3	0	···	···	40			···

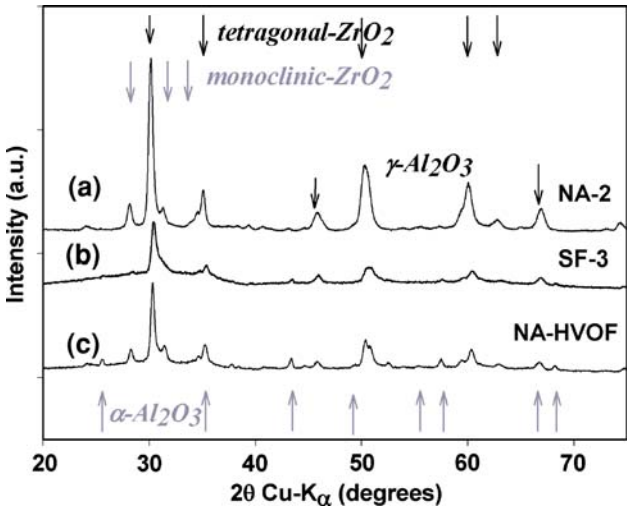

Fig. 7 XRD spectra of selected coatings, showing amorphous and crystalline components

lamellae along with uniformly dispersed fine-grained ZrO_2 features, indicating incomplete melting of the original nanosized zirconia. This complex structure is reflected in the XRD analysis, with an amorphous phase content of 48% and the presence of stable (α-Al_2O_3, m-ZrO_2) and metastable phases (γ-Al_2O_3 and t'-ZrO_2). Ultimately, some incomplete melting of the refractory feedstock in the relatively low flame temperature HVOF is expected (Ref 34). The larger grain sizes in this coating, as compared to the plasma-sprayed coatings, also suggest a lower particle temperature, at least inside the droplet, before solidification on the substrate, which may lead to a less intimate particle bonding in the coating. It should be mentioned that the HVOF coatings exhibit a lower degree of macroscopic defects or arborescence, which may be related to a highly collimated particle jet and surface bombardment by unmelted particles.

3.3 In-flight Particles and Coating Morphology

The plasma-sprayed coatings from the NA and the SF feedstock powders show a remarkable difference in phase and microstructure, which requires further explanation. While the SF coatings contain a high degree of Al_2O_3-ZrO_2 alloying and amorphous phase, the NA coatings are nearly entirely crystalline with limited dissolution of the primary alumina and zirconia powders. The formation of the distinct compositional layers is somewhat nonintuitive, since the smaller nanosized constituents of the NA feed allow, in principle, a more intimate mixing of the ceramics. However, the complex mechanism of particle creation in the plasma jet can vary drastically with particle size and distribution in the suspension (Ref 35) and is here further explored.

Figure 8 shows the size distribution of free-flight particles created during the plasma spray process for conditions NA-2 and SF-3, as collected in a water chamber. It is interesting to note that the shape and values of the principal size distribution peaks of the sprayed free-flight particles are similar to the aggregate distribution in the corresponding suspension feed (see Fig. 3). For the nanosized NA particles, the normal distribution of the agglomerate size is to some extent preserved and the median value is shifted only from 5.83 to 5.08 μm. This could indicate that the ceramic droplets are constituted from the original agglomerates. For the super-fine SF particles on the other hand, a sharper size distribution with a maximum value at approximately 2 μm can be recognized in both the feed and the overspray, while a minor peak of submicron particles has disappeared. A possible interpretation is the presence of aggregates of around 2 μm size (alumina) in the feed, which amass the submicron particles (zirconia) to form individual molten droplets. Delbos et al. (Ref 35) studied the influence of powder size distribution on splat formation and suggest that for large attrition-milled zirconia powders, each original powder particle can form a single splat. However, the free-flight particle distributions also feature shoulders of much larger particles, which may have formed by additional agglomeration and particle interaction. Nonetheless, the original nanoparticle agglomerates appear to play an important role in their transformation into ceramic droplets during the solvent evaporation step. It is worthwhile to note that the in-flight particles from the submicron feed (SF) are smaller than those from the nanosized feed (NA), which may explain the higher in-flight particle velocities and slightly higher propensity to conical porous defect formation in the SF samples.

Polished cross sections of in-flight collected particles from the NA feedstock are shown in Fig. 9, displaying a core-shell structure with an alumina-rich core and

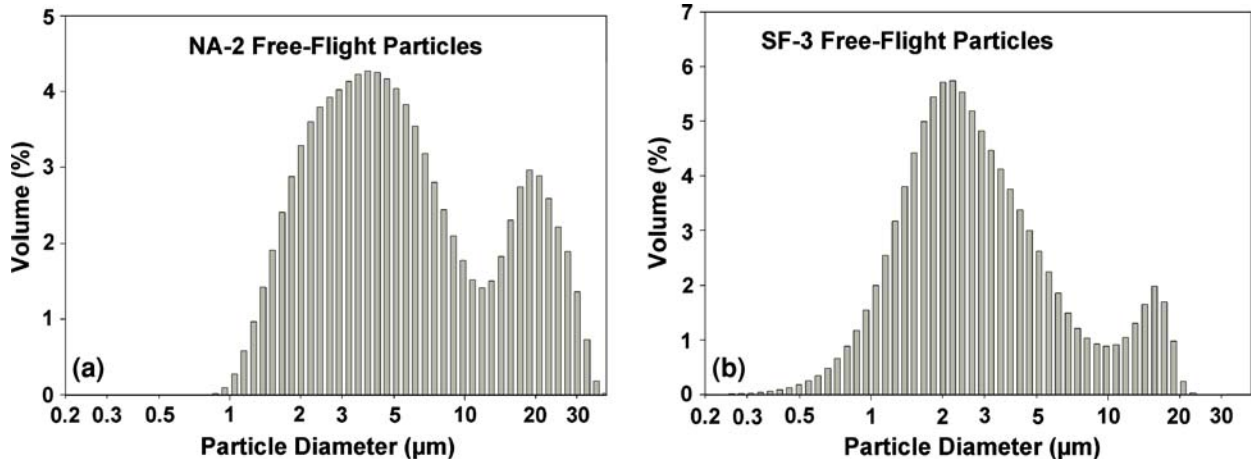

Fig. 8 Free-flight particle size distribution for typical plasma spray conditions using (a) nanosized feedstock powder NA and (b) superfine feedstock powder SF

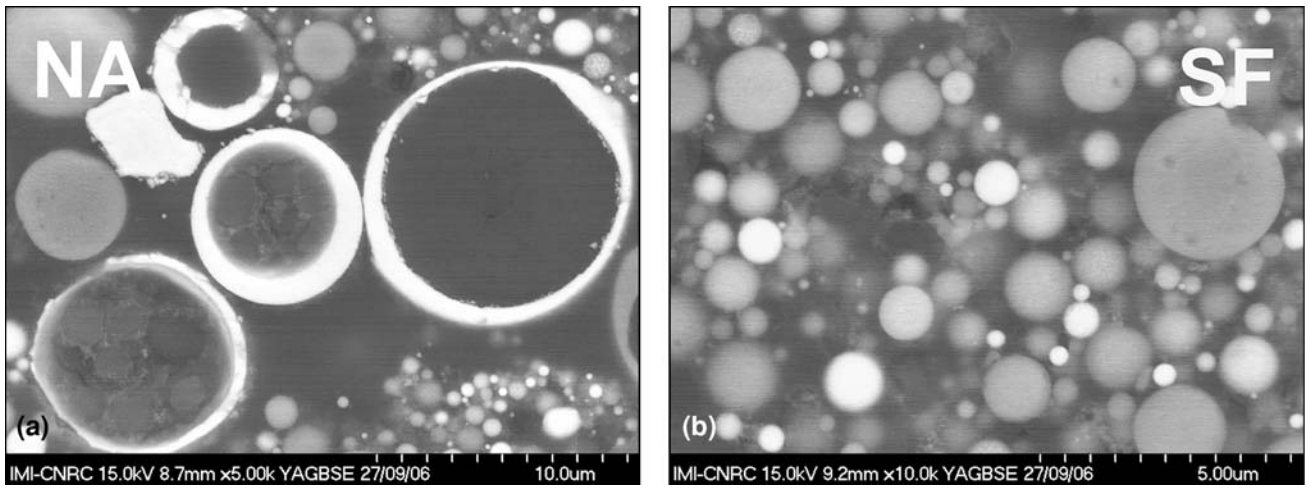

Fig. 9 Cross section of in-flight particles from (a) nanosized suspension feed NA-2 showing core-shell morphologies with a zirconia-rich shell and alumina-rich core and (b) submicron suspension feed SF-3, showing homogenous phase distribution in the particles

zirconia-rich shell. Only particles larger than 2 μm were successfully cleaved due to limitations in the polishing media. The core of the particles appears porous or even hollow in some cases. During evaporation of the solvent, the ceramic concentration builds up near the droplet surface to form a concentrated ceramic shell as the droplet shrinks. This layer may inhibit further diffusion of the solute (ethanol) and delay complete melting. Ozturk et al. describe a similar mechanism in liquid precursor thermal spraying and delineate the conditions leading to hollow sphere particles (Ref 36). A unique feature here is the segregation of the ceramic within a droplet into the zirconia-rich shell and alumina-rich core. It can be speculated that the segregation is caused by a higher affinity of zirconia to the solvent (over alumina), allowing the solvent to entrain the zirconia particles as it flows from the center to the outside of the droplet during evaporation. The melting and mixing of the molten ceramics is limited by this driving force for segregation, the reduced heating of the particle core, and the short residence time of the droplet in the plasma jet.

The free-flight particles from the SF feedstock, on the other hand, have a homogenous composition and no shell-like particles were found. Typical particles are shown in Fig. 9(b). For the SF feed, the larger primary particles in the center of the suspension droplet likely reduce entrapment of the solvent in the core and are less easily entrained ensuring more homogenous melting and mixing of the ceramic. Rapid quenching of those homogenous particles on a substrate is expected to promote an amorphous phase in the resulting coating (Fig. 5b).

For the core-shell particles, the segregated microstructure is likely retained until impact. Top-view SEM images of impacted particles, as depicted in the example in Fig. 10, show zirconia (white-contrast) only at the very edges of some splats. A bilayer structure with the

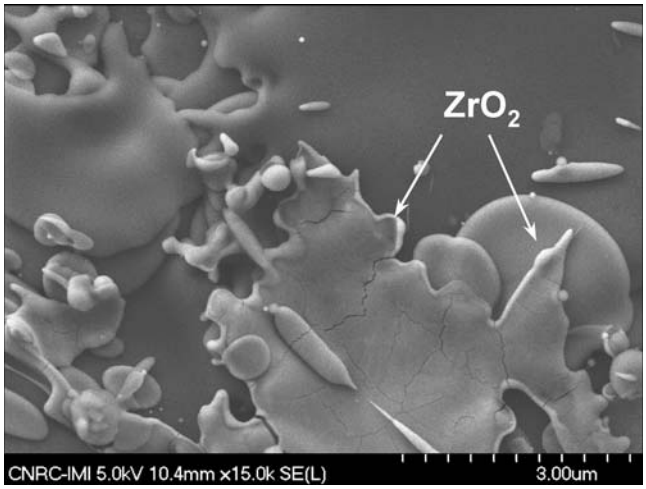

Fig. 10 Top-view SEM image of splats form nanosized feed suspension NA, showing white zirconia contrast only at the splat edges and suggesting a bilayer splat structure

zirconia-rich material on the underside of the splat is possibly created, which is consistent with the observed microstructure.

3.4 Mechanical Behavior and Properties

Selected mechanical properties, such as hardness, abrasion and erosion volume loss of the suspension-sprayed alumina-zirconia composite coatings were evaluated. The hardness values in Fig. 11 show that the compositionally segregated coatings from the nanosized NA feedstock are generally harder than the coatings with the amorphous phase content, as created from the submicron SF powder. The coating NA-2 with 1125 $VHN_{3\ N}$ is the hardest in this study. Besides a low porosity in the bulk of the coating, the nanosized crystal grains (smaller than 30 nm) can contribute to this high hardness in accordance with the Hall-Pecht relationship (Ref 15). The superior hardness of NA-2 over the NA-1 coating may be the result of the layer refinement and improved splat contact, induced by the higher particle temperature and velocity, as seen in Fig. 5 and 6. With further increase in velocity, the hardness somewhat decreases in coating NA-3, possibly because of the incorporated in-flight solidified particles, leading to a less-defined lamellar structure and compromised splat contact. It should be pointed out that the measured hardness exceeds the values reported for conventional plasma (APS)-sprayed Al_2O_3-40% ZrO_2 coatings (Ref 37, 38) and approaches those of APS-sprayed alumina, at similar macroscopic porosity. The SF-3 coating shows a lower hardness value, which is likely due to the presence of the weak amorphous phase. Even though exceptionally high hardness values are reported for pseudo-binary Al_2O_3-ZrO_2 alloys produced by plasma spraying (Ref 13, 15), these values are generally obtained only after heat-treatment and crystallization into a nanocomposite of the as-sprayed coatings. The HVOF-sprayed composite has the lowest hardness, containing both a

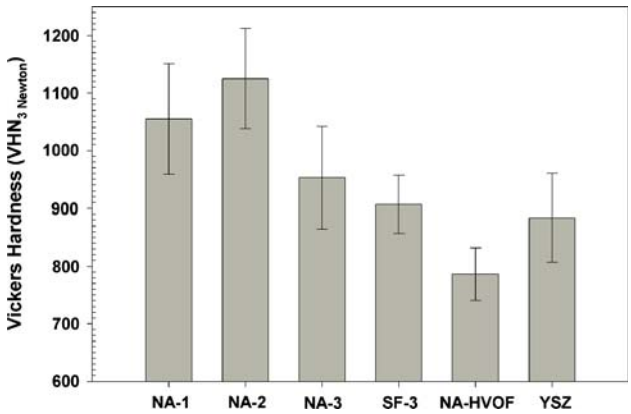

Fig. 11 Hardness $VHN_{3\ N}$ for selected coatings, showing hardest plasma-sprayed coatings from nanosized NA feedstock and softest coating by HVOF spraying. Error bars represent standard deviations resulting from 10 non-adjusted measurements

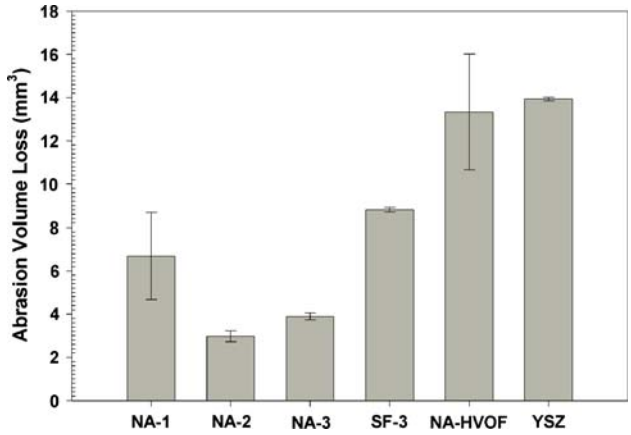

Fig. 12 Abrasion wear volume loss (ASTM G-65). Error bars represent standard deviations resulting from three non-adjusted measurements

softer amorphous phase and dispersed unmolten zirconia particles with possibly weak particle bonding.

Figure 12 shows the abrasion volume loss of the coatings as measured with a modified ASTM-65 method. The hard NA-2 coating shows the best abrasion resistance in this study. The slightly softer coatings NA-1 and NA-3 show lower wear performance. This is followed by the amorphous SF-3 coating. The lowest resistance is found for the HVOF-sprayed coating and the YSZ reference coating, which also showed the lowest hardness values. The direct relation between hardness and abrasion volume loss is in accordance with abrasive wear behavior of ceramic bulk materials (Ref 38, 39).

Figure 13 summarizes the volume loss under dry particle erosion at an angle of 30° according to ASTM G-75. Contrary to the superior abrasion performance of the compositionally segregated coatings (NA-1 to NA-3), they show only an intermediate resistance against dry particle erosion. The lowest erosion resistance was measured for

the amorphous SF-3 coating, while the highest resistance is shown by the rather soft NA-HVOF and YSZ coatings. Contrary to the expected behavior of bulk ceramics (Ref 39), the erosion resistance does not rank with the hardness values in our case. The high hardness may come at the expense of increased brittleness in some coatings, which may adversely affect their erosion wear behavior. Figure 14 shows crack formation on the corners of the Vickers indent impressions in the segregated NA-2 and amorphous SF-3 coating, while the NA-HVOF coating is virtually crack free (Ref 3). The crack propagation resistance, which can serve as an indication of the toughness of the material, was determined from the average crack length originating from the corners of the Vickers indentation impression and is summarized in Fig. 15. It can be noted that the erosion wear volume loss ranks closely with the crack propagation resistance. The low toughness of the amorphous SF-3 coating leads to the low erosion resistance, followed by the compositionally segregated NA-2 coating. The highest toughness values are measured in the HVOF (NA-HVOF) coating and the zirconia (YSZ), translating into superior erosion wear resistance. The high toughness of partially stabilized zirconia is well documented and is related to the transformation of metastable t-ZrO_2 into m-ZrO_2 in the stress

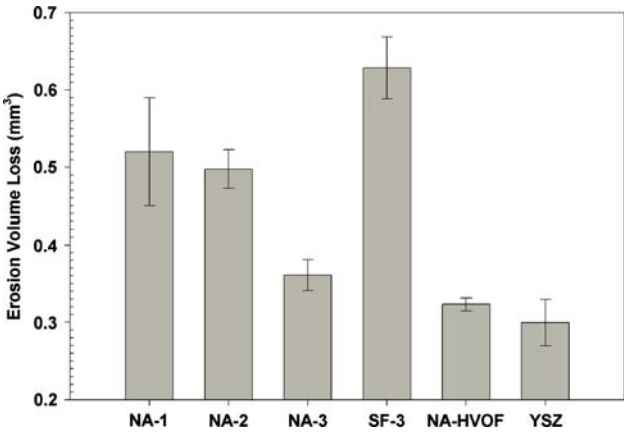

Fig. 13 Erosion wear volume loss as measured at 30° particle impingement (ASTM G-75). Error bars represent standard deviations resulting from three non-adjusted measurements

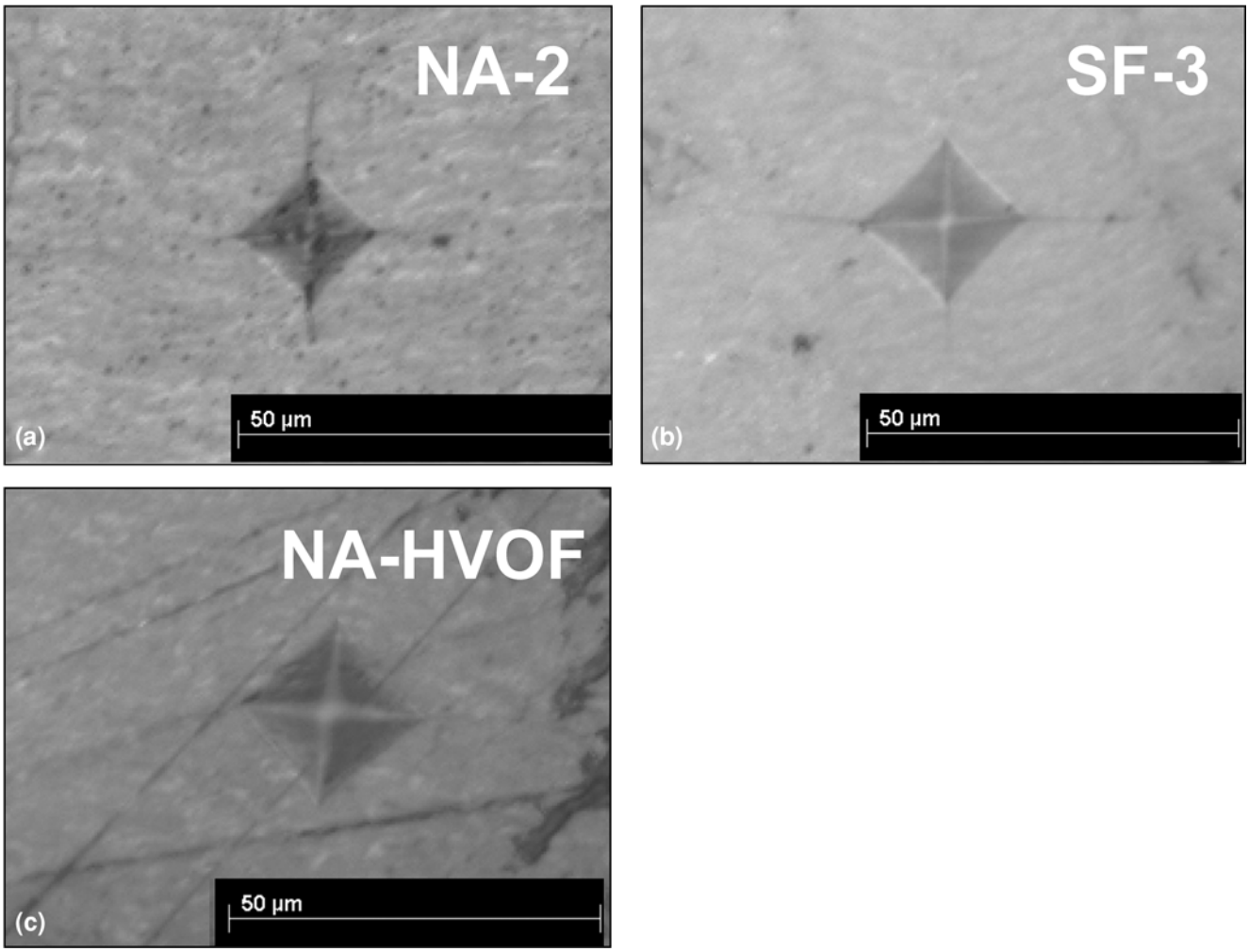

Fig. 14 Optical images of Vickers indent impression at 300 g load in coating (a) NA-2 and (b) SF-3, showing extensive crack formation emanating from the indent corners parallel and perpendicular to substrate surface, and (c) NA-HVOF, showing virtual absence of cracks

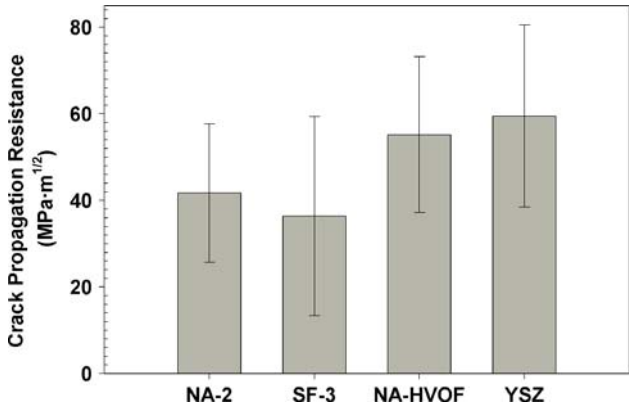

Fig. 15 Estimated crack propagation resistance of selected coatings, showing superior toughness in partially stabilized zirconia and HVOF-sprayed Al_2O_3-40 ZrO_2. Error bars represent standard deviations resulting from at least 40 non-adjusted measurements

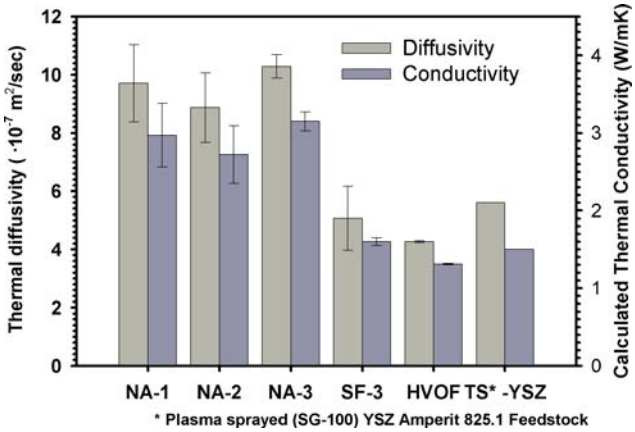

Fig. 16 Thermal diffusivity and estimated conductivity of selected coatings, showing highest thermal resistance in plasma-sprayed SF and HVOF-sprayed Al_2O_3-40 ZrO_2 coatings. Error bars represent standard deviations resulting from at least four non-adjusted measurements. Material densities were approximated by a linear mixing law, neglecting porosity

field at a crack tip. This transformation exerts local compressive stresses, due to a volume expansion, hindering further crack propagation (Ref 6). The superior toughness of the HVOF-coating may be related to the finely dispersed unmolten tetragonal and monoclinic ZrO_2 particles in the Al_2O_3 and Al_2O_3-ZrO_2 alloy matrix, as has been illustrated by Claussen et al. (Ref 40, 41). The second phase acting as crack arrestors and the propagation of microcracks in a large zone in front of the crack tip due to the phase transformation in small zirconia particles can be made responsible for this increase in toughness.

3.5 Thermal Transport Properties

The thermal diffusivities of the coatings are compared in Fig. 16. The compositionally layered coatings NA-1 to NA-3 show the highest diffusivity and conductivity values. Intuitively, the high number of alumina/zirconia interfaces could be expected to induce some resistance to thermal transport. However, the conductivities between 2.7 and 3.15 W/m K for the NA coatings correspond closely to values reported for small-particle plasma-sprayed Al_2O_3-ZrO_2 laminates, of similar overall composition, with much fewer interfaces, i.e., 40 distinct interfaces as reported by Su et al. (Ref 42). Using a thermal conductivity k of 24 W/m K for bulk Al_2O_3 and 2.2 W/m K for YSZ (Ref 8), the measured values here are only a little lower than can be calculated for a multilayer material using a series heat transfer model, and assuming a fully dense material, with volume fraction υ and materials 1 and 2, as follows:

$$k_{ML} = (k_1 k_2)/(\upsilon_1 k_2 + \upsilon_2 k_1) \quad \text{(Eq 1)}$$

This equations yields k_{ML} of 5.89 W/m K for a 60% Al_2O_3/ZrO_2 multilayer (Ref 42). This calculation suggests that the alumina/zirconia interfaces play a minor role in thermal resistivity, as has been shown by Ravichandran et al. (Ref 7). In conventional plasma-sprayed TBCs a low thermal diffusivity is generally attributed to the porosity and fine gaps at the interfaces of the individual splats, acting as local thermal resistances. The suspension plasma-sprayed coatings, on the other hand, show a very intimate splat contact and very low porosity, leading to little thermal transport resistance.

A significant reduction in diffusivity is measured for the SF-3 and HVOF coatings, both of which contain a high degree of amorphous phase. The glassy phases and the enclosed nucleated nanograins (smaller than 50 nm) are often made responsible for enhanced phonon scattering at room temperature (Ref 14, 43). The lowest diffusivity was measured for the HVOF coating, which not only has an amorphous phase components, but also incorporates nanoporous zones of unmolten zirconia with limited particle bonding, as mentioned earlier. The thermal transport properties of these coatings are comparable to commercial plasma-sprayed TBCs, as shown for Amperit 825.1 feedstock (H.C. Stark Inc, Cleveland, OH, USA) sprayed with a Praxair SG-100 (Praxair, Mississauga, Canada) torch at standard conditions.

4. Conclusions

- Al_2O_3-ZrO_2 microlaminates and nanocomposites were produced by suspension thermal spraying of submicron feedstock powders using air plasma (APS) and supersonic flame (HVOF) spray technologies. The suspensions were axially injected into the torch/gun interior. Optimized spray parameters were necessary to reduce the occurrence of large porous and arborescant defects. High in-flight particle temperatures and velocities, as measured with a particle diagnostic system, were employed to create continuous coatings with porosities below 2%.
- Two different submicron feedstock powders were compared for plasma spraying. It was found that the smaller nanopowders can create fine laminates of

alumina and zirconia layers, while slightly larger powders promote pseudo-alloyed Al_2O_3-ZrO_2 amorphous phase components. The unique microstructures of the finely segregated layers are a consequence of a complex mechanism of particle formation in the atomization and solvent evaporation step. The aggregates of the nanopowder produce droplets of core-shell structure with an alumina-rich core and a zirconia-rich shell. The incomplete mixing within the droplets is retained until impact on the substrate. It was further observed that the in-flight particle size, which is a critical parameter in the coating formation, is closely linked to the aggregate size in the suspension and was different for the two powders.

- HVOF spraying of ceramic nanopowder suspensions was successfully implemented. The lower flame temperature allows retention of some of the size features and phases of the feedstock, leading to complex microstructures containing amorphous as well as unmolten feedstock components.
- Mechanical properties of the coatings were compared. Compositionally segregated crystalline coatings, obtained by plasma spraying, showed the highest hardness of up to 1125 $VHN_{3\ N}$, as well as the highest abrasion wear resistance (ASTM G65). Their erosion wear performance was, however, compromised by their brittleness. The more amorphous plasma spray coatings were both softer and more brittle, leading to rather poor wear performance. The HVOF coatings were neither very hard nor particularly abrasion resistant, but they exhibited the highest erosion wear resistance (ASTM G75), which was related to the toughening effect of small dispersed zirconia particles in the alumina-zirconia-alloyed matrix.
- The HVOF composites exhibited the lowest thermal diffusivity due to a high amorphous phase content, limited particle bonding, and incorporation of partially molten feedstock at the low flame temperature. The alumina/zirconia interfaces in the segregated plasma-sprayed coatings pose only a small resistance to thermal transport, leading to high diffusivity values. It was observed that an amorphous/nanocomposite structure from a pseudo-alloyed phase constitutes the principal resistance to thermal transport in these coatings.
- A large variety in microstructures and properties of suspension-sprayed Al_2O_3-ZrO_2 composites was induced by the different feedstocks, spray systems, and operating conditions. This flexibility is expected to allow tailoring and optimization of these coatings to meet desired property requirements in the future, which is the focus of our ongoing work.

Acknowledgments

This work was supported through the collaborative program on Amorphous and Nanocrystalline Ceramic Coatings (ANCEC) between the National Research Council of Canada and the Academy of Science of the Czech Republic.

References

1. S. Deb and B.V. Radhakrishna Bhat, Optimization of Processing Parameters for making Alumina-Partially Stabilized Zirconia Laminated Composites, *Bull. Mater. Sci.*, 2000, **23**(2), p 109-117
2. D.J. Green, P.Z. Cai, and F.L. Messing, Residual Stresses in Alumina-Zirconia Laminates, *J. Euro. Ceram. Soc.*, 1999, **19**(13/14), p 2511-2517
3. A. Dakskobler and T. Kosmac, The Preparation and Properties of Al_2O_3-ZrO_2 Composites with Corrugated Microstructures, *J. Euro. Ceram. Soc.*, 2004, **24**(12), p 3351-3357
4. M. Jimenez-Melendo, F. Gutierrez-Mora, and A. Dominguez-Rodriguez, Effect of Layer Interfaces on the High-Temperature Mechanical Properties of Alumina/Zirconia Laminate Composites, *Acta Mater.*, 2000, **48**(18-19), p 4715-4720
5. H.M. Chan, Layered Ceramics: Processing and Mechanical Behavior, *Annu. Rev. Mater. Sci.*, 1997, **27**, p 249-282
6. V. Teixeira, A. Monteiro, J. Duarte, and A. Portinha, Deposition of Composite and Nanolaminate Ceramic Coatings by Sputtering, *Vacuum*, 2002, **67**, p 477-483
7. K.S. Ravichadran and K. An, Thermal Conductivity of Plasma-sprayed Monolithic and Multilayer Coatings of Alumina and Yttria-Stabilized Zirconia, *J. Am. Ceram. Soc.*, 1999, **82**(3), p 673-682
8. S. Sharafat, A. Kobayashi, Y. Chen, and N.M. Ghoniem, Plasma Spraying of Microcomposite Thermal Barrier Coatings, *Vacuum*, 2002, **65**, p 415-425
9. T. Kuroda and A. Kobayashi, Adhesion Characteristics of Zirconia-Alumina Composite Coatings by Gas Tunnel Type Plasma Spraying, *Vacuum*, 2004, **73**, p 635-641
10. A. Kobayashi, Formation of TiN-Al_2O_2-ZrO_2 Composite Coatings by Gas Tunnel Type Plasma Spraying, *Thermal Spray Connects: Explore its Surface Potential*, C. Berndt and E. Lugscheider, Eds., May 2-4, 2005 (Basel, Switzerland), ASM International, 2005
11. X. Zhou, V. Shukla, W.R. Cannon, and B.H. Kear, Metastable Phase Formation in Plasma-Sprayed ZrO_2 (Y_2O_3)-Al_2O_3, *J. Am. Ceram. Soc.*, 2003, **86**(8), p 1415-1420
12. H.-J. Kim and Y.J. Kim, Amorphous Phase Formation of the Pseudo-Binary Al_2O_3-ZrO_2 Alloy during Plasma Spray Processing, *J. Mater. Sci.*, 1999, **34**, p 29-33
13. S. Sodeoka, M. Suzuki, and T. Inoue, Mechanical Properties of Plasma Sprayed Alumina-Zirconia Nano-Composite Films, *Thermal Spray: Building on 100 Years of Success*, B. Marple, M. Hyland, Y.-C. Lau, R. Lim, and J. Voyer, Eds., May 15-18, 2006 (Seattle, USA), ASM International, 2006
14. S. Sodeoka, M. Suzuki, and T. Inoe, Thermal and Mechanical Properties of Alumina-Zirconia Nano-Composite Coatings, Thermal Spray Solutions: Advances in Technology and Application, ASM International, May 10-12, 2004 (Osaka, Japan), ASM International, 2004
15. T. Chraska, K. Neufuss, J. Dubský, J. Nohava, and J. Oberste Berghaus, Plasma Spraying of a Novel Material with Amorphous and Nanocrystalline Microstructure, *Thermal Spray Connects: Explore its Surface Potential*, C. Berndt and E. Lugsheider, Eds., May 2-4, 2005 (Basel, Switzerland), ASM International, 2005
16. S. Deville, J. Chevalier, G. Fantozzi, J.-F. Bartolomé, J. Rquena, J.S. Moya, R. Torrecillas, and L.A. Díaz, Low-Temperature Ageing of Zirconia-Toughened Alumina Ceramics and its Implication in Biomedical Implants, *J. Euro. Ceramic Soc.*, 2003, **23**, p 2975-2982
17. J. Karthikeyan, C.C. Berndt, S. Reddy, J.-Y. Wnag, A.H. King, and H. Hermann, Nanomaterial Deposits Formed by DC Plasma Spraying of Liquid Feedstocks, *J. Am. Ceram. Soc.*, 1998, **81**(1), p 121-128
18. E.H. Jordan, L. Xie, X. Ma, M. Gell, N.P. Padture, B. Cetegen, A. Ozturk, J. Roth, T.D. Xiao, and P.E.C Bryant, Superior Thermal Barrier Coatings Using Solution Precursor Plasma Spray, *J. Therm. Spray Technol.*, 2004, **13**(1), p 57-65

19. B.G. Ravi, S. Sampath, R. Gambino, P.S. Devi, and J.B. Parise, Plasma Spray Synthesis from Precursors: Progress, Issues and Considerations, *Thermal Spray: Building on 100 Years of Success*, B. Marple, M. Hyland, Y.-C. Lau, R. Lim, and J. Voyer, Eds., May 15-18, 2006 (Seattle, USA), ASM International, 2006
20. P. Bazdell and S. Kuroda, Plasma Spraying of Submicron Ceramic Suspensions Using a Continuous Ink Jet Printer, *Surf. Coat. Technol.*, 2000, **123**, p 239-246
21. P. Fauchais, Understanding Plasma Spraying, *J. Phys. D: Appl. Phys.*, 2004, **27**, p R86-R108
22. R. Siegert, J.-E. Döring, J.-L. Marqués, R. Vaßen, D. Sebold, and D. Stöver, Influence of the Injection Parameters on the Suspension Plasma Spraying Coating Properties, *Thermal Spray Connects: Explore Its Surface Potential*, C. Berndt and E. Lugsheider, Eds., May 2-4, 2005, (Basel, Switzerland), ASM International, 2005
23. C. Delbos, J. Fazilleau, V. Rat, J.-F. Coudert, P. Fauchais, and L. Bianchi, Finely Structured Ceramic Coatings Elaborated by Liquid Suspension Injection in a DC Plasma Jet, *Thermal Spray Solutions: Advances in Technology and Application,* ASM International, May 10-12, 2004 (Osaka, Japan), ASM International, 2004
24. J. Oberste Berghaus, S. Bouaricha, J.-G. Legoux, and C. Moreau, Suspension Plasma Spraying of Nanoceramics Using an Axial Injection Torch, *Thermal Spray Connects: Explore its Surface Potential*, C. Berndt and E. Lugsheider, Eds., May 2-4, 2005, (Basel, Switzerland), ASM International, 2005
25. A.L. Vasiliev, N.P. Padture, and X. Ma, Coatings of Metastable Ceramics Deposited by Solution-Precursor Plasma Spray: I. Binary ZrO_2-Al_2O_3 System, *Acta Mater.*, 2006, **54**, p 4913-4920
26. J. Oberste Berghaus, S. Bouaricha, J.-G. Legoux, and C. Moreau, Injection Conditions and In-Flight Particle States in Suspension Plasma Spraying of Alumina and Zirconia Nano-Ceramics, *Thermal Spray Connects: Explore its Surface Potential*, C. Berndt and E. Lugsheider, Eds., May 2-4, 2005 (Basel, Switzerland), ASM International, 2005
27. G.R. Anstis, P. Chantikul, B.R. Lawn, and D.B. Marshall, A Critical Evaluation of Indentation Techniques for Measuring Fracture Toughness. I. Direct Crack Measurements, *J. Am. Ceram. Soc.*, 1981, **64**(9), p 533-538
28. "Standard Test Method for Measuring Abrasion Using the Dry Sand/Rubber Wheel Apparatus," G 65-91, *Annual Book of ASTM Standards*, ASTM, 1993, p 363-368
29. "Standard Practice for Conducting Erosion Tests by Solid Particle Impingement Using Gas Jets," G 75-89, *Annual Book of ASTM Standards*, ASTM, 1989, p 305-309
30. A.S. Houlbert, P. Cielo, C. Moreau, and M. Lamontagne, Measurement of Thermal Diffusivity and anisotropy of Plasma-Sprayed Coatings, *Int. J. Thermophys.*, 1994, **15**(3), p 525-546
31. B.D. Cullity, Elements of X-Ray Diffraction, (2nd ed.). Addison-Wesley Publ. Co, Massachusetts, 1978
32. R.W. Trice and K.T. Faber, Role of Lamellae Morphology on the Microstructural Development and Mechanical Properties of Small-Particle Plasma-Sprayed Alumina, *J. Am. Ceram. Soc.*, 2000, **83**(4), p 889-896
33. J. Oberste Berghaus, S. Bouaricha, J.-G. Legoux, C. Moreau, R. Hui, and D. Gosh, Suspension Plasma Spraying of Intermediate Temperature SOFC Components using an Axial Injection DC Torch, *Materials Science Forum*, Vols. 539-543, Trans Tech Publications, March 2007
34. A. Killinger, M. Hyhn, and R. Gadow, High-Velocity Suspension Flame Spraying, A New Approach for Spraying Nanoparticles with Hypersonic Speed, *Surf. Coat. Technol.*, 2006, **201**, p 1922-1929
35. C. Delbos, J. Fazilleau, V. Rat, J.-F. Coudert, P. Fauchais, and L. Bianchi, Influence of Powder Size Distribution and Heat Flux on Yttria Stabilized Coatings Elaborated by Liquid Suspension Injection in DC Plasma Jet, *Thermal Spray Connects: Explore its Surface Potential*, C. Berndt and E. Lugsheider, Eds., May 2-4, 2005, (Basel, Switzerland), ASM International, 2005
36. A. Ozturk and B.M. Cetegen, Modeling of Plasma Assisted Formation of Precipitates in Zirconium Containing Liquid Precursor Droplets, *Mater. Sci. Eng. A*, 2004, **384**, p 331-351
37. G. Barbezat, A.R. Nicoll, and A. Sickinger, Abrasion, Erosion and Scuffing Resistance of Carbide and Oxide Ceramic Thermal Sprayed Coatings for Different Applications, *Wear*, 1993, **162-164**(pt. A), p 529-537
38. A.A. Abdel-Samad, A.M.M. El-Bahloul, S.A. Rassoul, and E. Lugscheider, A Comparative Study on Thermally Sprayed Alumina Based Ceramic Coatings, *J. Mater. Sci.*, 2000, **35**(12), p 3127-3130
39. H.X. Zhao, H. Goto, M. Matsumura, T. Takahashi, and M. Yamamoto, Slurry Erosion of Plasma-sprayed Ceramic Coatings, *Surf. Coat. Technol.*, 1999, **115**(2-3), p 123-131
40. N. Claussen, Fracture Toughness of Al_2O_3 with an Unstabilized ZrO_2 Dispersed Phase, *J. Am. Ceram. Soc.*, 1976, **59**(9), p 49
41. W.H. Tuan, R.Z. Chen, T.C. Wang, C.H. Cheng, and P.S. Kuo, Mechanical Properties of Al_2O_3/ZrO_2 Composites, *J. Euro. Ceram. Soc.*, 2002, **22**(16), p 2827-2833
42. Y.J. Su, H. Wang, W.D. Porter, A.R.A. Lopez, and K.T. Faber, Thermal Conductivity and Phase Evolution of Plasma-sprayed Multilayer Coatings, *J. Mater. Sci.*, 2001, **36**(14), p 3511-3518
43. S. Raghavan, H. Wang, R.B. Dinwiddie, W.D. Porter, and M.J. Mayo, The Effect of Grain Size, Porosity and Yttria Content on the Thermal Conductivity of Nanocrystalline Zirconia, *Scripta Mater.*, 1998, **39**(8), p 1119-1125